JOURNAL OF GEOPHYSICAL RESEARCH, VOL. 103, NO. C6, PAGES 12,839–12,852, JUNE 15, 1998

Radar-derived interferometric surface currents and their relationship to subsurface current structure

Delwyn Moller[1] and Stephen J. Frasier
Microwave Remote Sensing Laboratory, University of Massachusetts, Amherst

David L. Porter
Applied Physics Laboratory, Johns Hopkins University, Laurel, Maryland

Robert E. McIntosh
Microwave Remote Sensing Laboratory, University of Massachusetts, Amherst

Abstract. Radar-derived ocean surface currents are analyzed in conjunction with in situ acoustic Doppler current profiler (ADCP) measurements. The interferometric measurements were collected by an X-band imaging Doppler radar in a manner analogous to those of along-track interferometric synthetic aperture radar (ATI-SAR). While the advent of ATI-SAR has provided a new, potentially powerful technique for current mapping, the relationship between surface currents and interferometric velocity measurements is not yet clearly understood. This paper presents comparisons between radar-derived and in situ current measurements. To develop a precise method for estimating the surface current from interferometric measurements, the influence of long wave orbital velocities and the influence of Bragg resonant waves are studied. We find that coupling between the orbital velocity and backscattered power (i.e., the modulation transfer function) can bias surface current estimates, potentially by up to 20 cm s^{-1} in an upwind viewing orientation. Furthermore, experimental observations verify a $\cos^{2n}(\theta/2)$ analytical model for the directional spreading of Bragg resonant waves. Extending our analysis to include subsurface currents, case studies are presented under varying environmental conditions for which the vertical current structure changes considerably. Analysis of radar imagery yields both radial surface currents and vector subsurface current estimates derived from long wave dispersion characteristics. Combining these with coincident ADCP measurements yields a vertical profile of current. Using these measurement techniques, we make several observations within the upper meter of the ocean. These profiles reveal the sensitivity of X-band interferometric measurements to wind-drift and the near-surface current structure.

1. Introduction

Radar remote sensing has been applied to measurement and mapping of ocean currents for many years. In particular, high-frequency (HF) [*Barrick*, 1972; *Stewart and Joy*, 1974; *Fernandez et al.*, 1996] and microwave (ΔK) systems [*Plant*, 1977; *Schuler*, 1978; *Alpers and Hasselmann*, 1978; *Popstefanija and McIntosh*, 1992] have shown great utility in their ability to provide near-surface current measurements averaged over large areas.

Most recently, however, the innovation of along-track interferometric synthetic aperture radar (ATI-SAR) [*Goldstein et al.*, 1989] demonstrated the potential for imaging of surface ocean currents with relatively fine spatial resolution and area coverage limited in the along-track direction only by the flight path. An ATI-SAR employs two SAR antennas spatially separated in the along-track direction to yield two complex SAR images. When coregistered, they are separated by a time lag equal to the antenna separation divided by the platform velocity. The covariance of the two images is an interferogram, the magnitude of which is akin to a conventional SAR image while the phase includes Doppler velocity information from which surface currents are derived.

ATI-SAR is a relatively new technique, and to date, there have been few quantitative comparisons of interferometric current measurements with environmental data [*Thompson and Jensen*, 1993; *Ainsworth et al.*, 1995; *Shemer et al.*, 1993; *Graber et al.*, 1996; *Marmorino et al.*, 1997]. With the exception of the latter studies (*Graber et al.* [1996] treated HF measurements as ground truth for the ATI-SAR, and *Marmorino et al.* [1997] compared changes in ATI-SAR-derived surface currents with ADCP measurements across frontal boundaries) the studies were limited by a lack of in situ sensors, especially within the context of the large spatial coverage of the ATI-SAR imagery and the difficulty of making near-surface current measurements.

Because of the deficit of comprehensive comparisons, interpreting the physical relevance of interferometric velocities is not straightforward. One difficulty in estimating surface currents is uncertainty in the net component of velocity due to

[1]Now at Jet Propulsion Laboratory, Pasadena, California.

Paper number 98JC00781.
0148-0227/98/98JC-00781$09.00

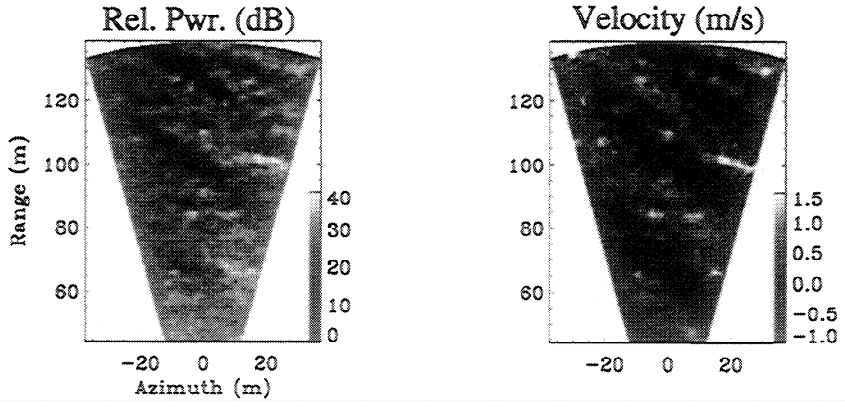

Figure 1. Typical focused phased array imaging radar (FOPAIR) imagery. (left) Backscattered power corrected for a cubic range dependence and the radar's antenna pattern. (right) The mean (0.25 s) surface velocities derived from the covariance phase of successive array scans.

Bragg resonant waves. In particular, for viewing orientations off the wind axis the relative contributions of both advancing and receding Bragg waves are not well known. *Thompson and Jensen* [1993] illustrated that this uncertainty can be a significant source of error, and although the conditions considered in that paper were rather specific, they demonstrated the severity of misinterpretation that occurs when incorrect assumptions are made. Commonly, ATI-SARs fly orthogonal overlapping paths to generate vector surface current maps; consequently, at least one of the flight lines must be oblique to the wind direction. For such an example, *Shemer et al.* [1993] addressed the Bragg uncertainty issue by extending the flight path over land to image a reservoir of standing water. This reservoir was subject to similar wind conditions but without the influence of current making this a convenient source for estimating the relative Bragg velocity. However, this was a unique situation, and more general solutions are needed.

In this paper the focused phased array imaging radar (FOPAIR) [*McIntosh et al.*, 1995] is used to study interferometric surface current measurements and their relationship to the surface and near-surface current structure. Like ATI-SAR, FOPAIR infers Doppler velocity from the covariance of successive complex radar images, but the comparatively small spatial coverage of this system makes it feasible to compare radar-derived current measurements with nearby in situ measurements. Surface currents are derived from radar measurements by removing the effects of both the wave orbital velocity and the net Bragg velocity. Utilizing in situ measurements, we examine both of these parameters in detail and suggest methods of correction. Most notably, the angular dependence of the net Bragg velocity compares favorably to a model for the angular spreading of short waves.

The remainder of the paper addresses the question of how representative surface currents as seen by an ATI-SAR are of the currents in the water column. The relationship of interferometric measurements to the subsurface current structure is explored by presenting case studies for differing environmental conditions. In addition to the surface velocity measurements, spectral analysis of FOPAIR imagery yields independent near-surface current estimates. The combination of radar-derived surface and near-surface currents and ADCP measurements results in uniquely detailed vertical profiles of the current.

An overview of experimental conditions, in situ sensors, and the FOPAIR radar are included in section 2. Section 3 outlines the components comprising a surface current measurement and illustrates the surface current estimation technique. Section 4 discusses how near-surface currents are inferred from the dispersion properties of gravity waves resolved in radar imagery. The combination of ADCP and radar-derived current measurements clearly show the current evolution, especially near the surface. Finally, section 5 consolidates the applicability of this work to ATI-SAR analysis with comparisons between ATI-SAR and FOPAIR interferometric surface currents. In one such case, consecutive orthogonal acquisitions permit vector surface current comparisons.

2. Experimental Overview and Sensor Description

2.1. FOPAIR Radar System

FOPAIR is an X-band phased array radar employing digital beamforming to synthesize two-dimensional imagery of the ocean surface. The FOPAIR antenna hardware consists of two transmit horns and two linear receiving arrays: one vertically polarized and the other horizontally polarized. This paper presents only vertically polarized backscatter as it is dominated by distributed Bragg scattering and is therefore comparable to typical ATI-SAR measurements.

In operation the transmit horn is pulsed, illuminating an area of the ocean surface. With each pulse a single element of the linear array receives the echo. Sixty-four pulses are required to scan the entire array, essentially capturing a "snapshot" of the ocean over the scan time (typically 0.64 ms, well within the decorrelation time for microwave backscatter at X band). The operating range is within the near field of the array, so a focusing correction must be applied to the backscattered returns. The data from each array scan are then transformed into a two-dimensional complex image by Fourier transforming each range gate over the 64 elements.

To generate Doppler velocity estimates, a second complex image is collected, separated from the first by a short interval, nominally 2.5 ms. The interval is selected to be small with respect to the decorrelation time, yet long enough to yield sufficient velocity sensitivity. An interferogram is generated by cross correlating the two complex images. Normally, cross correlations are accumulated for 0.25 s to reduce the measurement noise due to fading. Figure 1 shows example imagery of radar backscatter and Doppler velocity.

2.2. Experimental Operation

During May, 1996, FOPAIR was deployed at Duck, North Carolina, at the Army Corps of Engineers Field Research Facility (FRF). FOPAIR was installed on a rotating platform at the end of the FRF pier (see Figure 2). Available viewing angles were somewhat constrained by obstructions at the end of the pier but ranged from slightly toward shore to directly offshore. The imaged area was a 24° sector between ranges of 50 and 150 m, which correspond to grazing angles between 11° and 4°, respectively. In addition, on a few occasions the Environmental Research Institute of Michigan (ERIM) overflew the site with an X-band ATI-SAR.

Both the FRF and Johns Hopkins University/Applied Physics Laboratory (JHU/APL) collected meteorological data including wind speed and direction. The JHU/APL data were collected at 0.17 Hz and then averaged to provide 1-min time series. In situ sensors, including an array of pressure sensors at 8 m depth indicated in Figure 2, provided wave frequency and directional measurements.

An upward looking 1200-kHz ADCP, situated on the ocean floor east of the pier in 8 m of water, provided orthogonal current estimates in alongshore and cross-shore directions. The maximum range of this type of ADCP is 94% of the distance to the surface. The ADCP head was located 2 m off the bottom, allowing us to get within ~0.5 m of the ocean surface. The uppermost range bin was varied with the phase of the tide, and we used the closest bin to the surface with a measurement standard deviation <1 cm s^{-1}. (The standard deviation of a single ping is 6 cm s^{-1}. We averaged over 60 pings during 1-min intervals resulting in a standard deviation of <1 cm s^{-1}.)

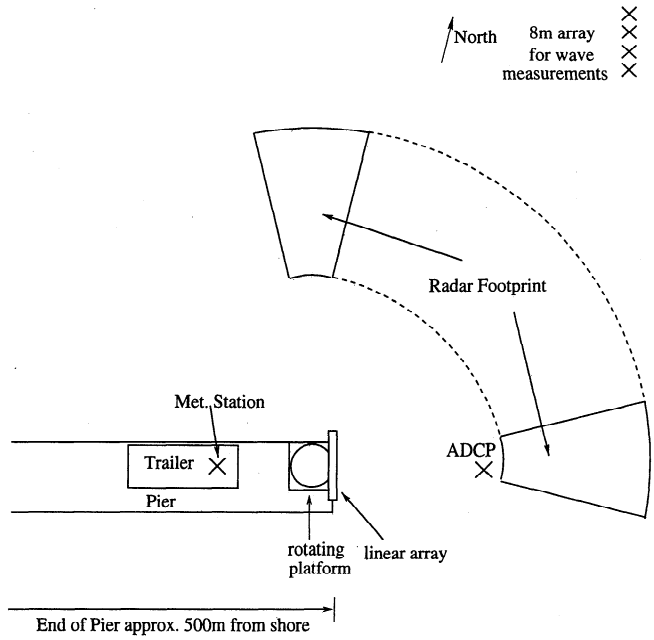

Figure 2. Experimental setup for the Field Research Facility (FRF) deployment. The radar hardware was housed in a trailer, except for the antenna hardware mounted on a rotating platform at the end of the pier. A meteorological station was installed on top of the trailer providing measurements of wind speed and direction. The acoustic Doppler current profiler (ADCP) was situated east of the pier end in ~8 m depth. The 8-m array provided wave directional measurements.

3. Radar-Derived Surface Velocity Measurements

Doppler velocity measurements are derived from the phase of the covariance of the backscattered field evaluated at a lag time, τ

$$\phi(t) = \arg C(t, \tau) \tag{1}$$

where $C(t, \tau)$ is defined as

$$C(t, \tau) = \langle I(t)I^*(t + \tau)\rangle_{0.25s} \tag{2}$$

$I(t)$ is the complex backscattered field at time, t, evaluated at each image pixel. The operator, $\langle\ \rangle_{0.25s}$, represents a coherent integration over 0.25 s. This integration time reduces the variance of the fading statistics but is short with respect to the period of the longer gravity waves, so the covariance is a time-varying quantity.

Assuming τ is less than the decorrelation time of the echo signal at the transmitted frequency, the phase of $C(t, \tau)$ is directly proportional to the mean Doppler frequency [*Miller and Rochwarger*, 1972]. The phase is converted to a velocity through

$$v(t) = \frac{\lambda}{2 \sin \theta_i} \frac{\phi(t)}{2\pi\tau} \tag{3}$$

where λ is the radar wavelength and θ_i is the incidence angle. The convention adopted here is that positive velocities represent movement toward the radar. Also, at near-grazing angles, $\sin \theta_i$ is close to unity.

An ocean surface Doppler velocity measurement is comprised of several contributing factors

$$v = U_c + U_d + v_o + v_b \tag{4}$$

where U_c represents a "bulk" water current due to a number of driving forces including but not limited to tidal currents, buoyant outflow from the Chesapeake Bay, and alongshore wind-driven flow. U_d is the surface wind drift current, v_o is the orbital velocity of the gravity waves, and v_b is the net velocity reported due to the phase velocities of Bragg-resonant waves. Bragg theory predicts a radar echo power proportional to the spectral density of radially traveling (i.e., both advancing and receding) resonant waves [*Plant*, 1990]. The net Doppler velocity due to these waves is the power-weighted sum of their oppositely signed phase velocities.

We consider a radial surface current, U_s, to consist of the first two terms of (4); that is, $U_s = U_c + U_d$. Thus, to extract the surface current from an interferometric or Doppler velocity measurement, the contributions of v_o and v_b must be extracted. In general, it is assumed that wave orbital velocities are irrotational and therefore average to zero over a number of wave periods. Later in this section, we demonstrate that coupling between the wave orbital velocity and backscattered power bias the average velocity and therefore the surface current estimate. The extent of this bias is sensitive to the radar orientation and the signal-processing approach used.

3.1. Azimuthal Dependence of Bragg Velocity

The phase speed of the Bragg-resonant capillary-gravity waves is given by

$$v_p = \sqrt{\frac{g}{|\mathbf{k}|} + \frac{\tau|\mathbf{k}|}{\rho}} \tag{5}$$

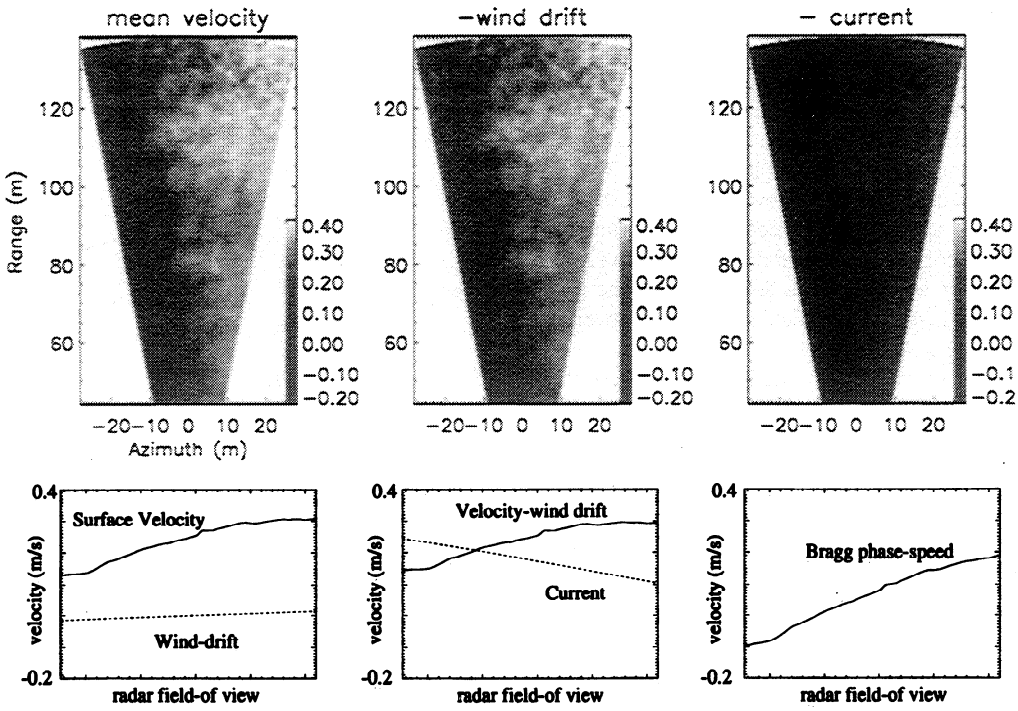

Figure 3. Method of estimating the Bragg-phase components of surface velocity measurements. (left) Mean velocity image with azimuthal profile and wind drift correction. (middle) Wind-drift-corrected image with azimuthal profile and current correction. (right) Residual velocity image with azimuthal profile.

where g is gravitational acceleration, τ is surface tension, ρ is water density, and $\mathbf{k}$ is the wavenumber of the Bragg-resonant waves [*Kinsman*, 1965]. At 10 GHz and near grazing incidence the Bragg-resonant wavelength is 1.5 cm, yielding a v_p of about 0.23 m s^{-1}. The velocity measured by the radar is dictated by the ratio of the spectral densities of advancing and receding waves within the resolution cell

$$v_b(\theta) = \alpha(\theta)v_p - [1 - \alpha(\theta)]v_p = [2\alpha(\theta) - 1]v_p \quad (6)$$

where α and $1 - \alpha$ represent the respective proportions of approaching and receding Bragg-resonant wave spectral density contributing to the radar echo. Since the Bragg waves at X band are assumed to follow the wind direction, when looking directly upwind, $\alpha = 1$ and $v_b = v_p$. Similarly, looking downwind, $\alpha = 0$ and $v_b = -v_p$. Off the wind axis, however, it is difficult to determine a value for v_b since α is unknown. To address this limitation, we estimated v_b across the radar field of view from our mean velocity measurements

$$v_b(\theta_w) = \langle v(\theta_w) \rangle - U_c(\theta_w) - U_d(\theta_w) \quad (7)$$

where θ_w is the angle between the radar boresight and the wind direction (0° = upwind). In situ ADCP measurements provide $U_c(\theta_w)$, and we approximate the wind drift, $U_d(\theta)$, by 3.5% of the radial component of wind speed at 10 m height,

$$U_d(\theta_w) = 0.035U_{10}(\theta_w) \quad (8)$$

Note that as discussed by [*Fernandez et al.*, 1996], wind-induced currents at the extreme surface are affected little by the Coriolis force, and therefore we assume no shift away from the wind direction.

Figure 3 demonstrates this procedure for one case. Figure 3 (left) shows a 10-min mean velocity image. The bottom of Figure 3 (left) shows the radial velocity profile across the image. This is a cross-wind example, so there is a notable trend over the field of view. Also included in this plot is the radial wind-drift component, which is small for cross wind. Figure 3 (middle) shows the mean velocity image after subtracting the wind drift, and the bottom of Figure 3 (middle) shows the radial profile across the image. Also included on the line plot is the current correction, U_c. Subtracting the current results in Figure 3 (right), which is the estimated net Bragg velocity. Note that in Figure 3 (right) there is still a significant azimuthal trend in the velocity. This is due to the variation across the field of view of the ratio of approaching to receding Bragg-resonant waves, thereby modulating v_b.

In this manner, measurements acquired throughout the 3-week experiment were processed to estimate v_b. These estimates encompass wind speeds ranging between 2 and 11 m s^{-1} and nearly the full range of wind aspect angles. Figure 4 illustrates the resulting azimuthal dependence of v_b for data pooled over all environmental conditions encountered. In Figure 4 the solid line is a model of v_b derived using a form for the angular dependence of the surface-wave spectral density [*Heron*, 1987; *Thompson*, 1989]

$$G(\theta_w) = \cos^{2n}\left(\frac{\theta_w}{2}\right) \quad (9)$$

where the exponent n is 2–5 in the intermediate region of the spectrum as detailed by *Lyzenga* [1991]. A close approximation to the data was achieved using $n = 4$.

Figure 5 illustrates how the directional dependence of v_b is determined from (9). Figure 5 (top) shows $G(\theta_w)$. Bragg scattering theory specifies that for a given viewing direction a radar is primarily sensitive to radially traveling waves satisfying the Bragg resonance condition. The selectivity of the radar to the surface spectrum is dictated by the size of the illuminated area

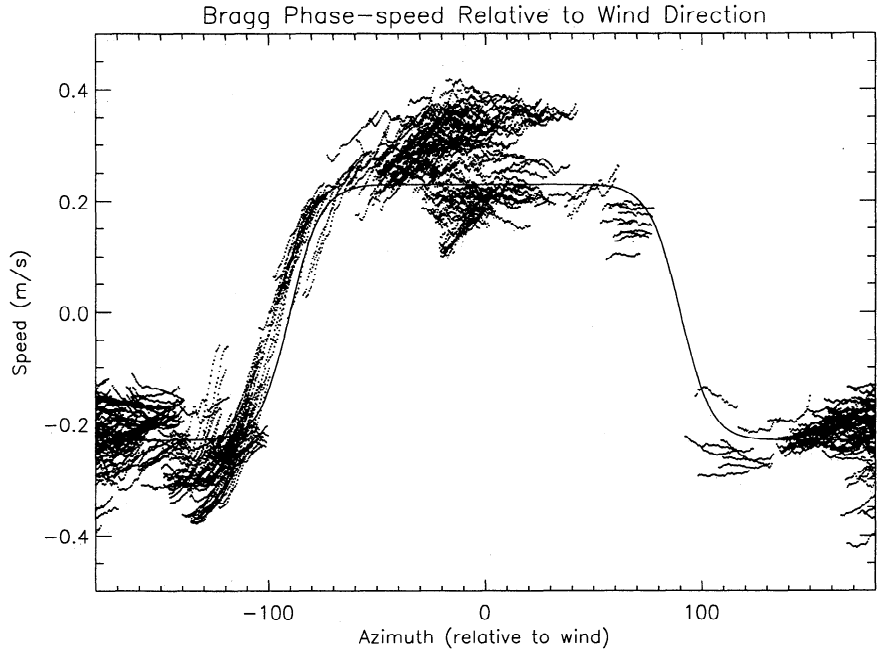

Figure 4. Estimated contribution of the Bragg-resonant waves to surface velocity measurements. The solid curve is a function approximating the azimuthal dependence of the Bragg contribution relative to wind direction.

relative to the Bragg scattering wavelength. The range cells of FOPAIR each incorporate about 100 Bragg wavelengths, enough to approximate the radar's effective spectral filter as a delta function at the resonant wavelength. The relative spectral densities of approaching and receding waves are used to determine v_b

$$v_b(\theta_w) = v_p\left[\frac{G(\theta_w) - G(\theta_w + \pi)}{G(\theta_w) + G(\theta_w + \pi)}\right] \tag{10}$$

Figure 5 (bottom) shows the v_b so calculated.

The measurements and the model suggest that to within ~60° of the wind axis, one may apply a Bragg correction which assumes waves traveling only in the positive radial direction. In these regions the estimates of v_b in Figure 4 experience a fair degree of variability about the expected value. We attribute this variability to the pooling of data over a variety of conditions using a common assumption for wind drift. To clarify, Figure 6 compares the wind speed dependence of upwind and downwind data with (8). The data shown are from within ±10° of upwind or downwind radar orientations, and therefore v_b is assumed to be 0.23 m s^{-1} traveling with the wind. The wind-drift component is estimated from

$$U_d = \langle v \rangle - v_p - U_c \tag{11}$$

Although the data follows (8), there is significant scatter about the expected relationship (O(10–20 cm s^{-1})). This variation is expected since the wind-drift relationship has shown significant variability in the literature ranging between 2.6 and 5.5% of the wind speed [*Lange and Huhnerfuss*, 1978] and is the same degree of variability that v_b exhibits in the upwind and downwind regions of Figure 4. The additional influence of non-Bragg scattering sources, particularly in the upwind orientation, also accounts for some of the scatter. While the degree of scatter may seem large, if the cause is indeed due to uncertainties in the wind drift, then this does not limit the overall accuracy of surface current estimates. The wind drift is indeed part of the surface current as it causes a net movement of surface water. In this light it is inconsequential whether or not the wind-drift current is consistently 3.5% of the wind.

3.2. Modulation Transfer Function Effects on Current Estimation

To extract the surface current from radar imagery, one approach is to assume that observed Doppler velocity modulations due to wave orbital velocities average to zero over a number of wave periods. This is rarely the case, however. First, fluid particles do not generally follow closed orbits, yielding a small net velocity in the wave direction (Stokes drift). From the radar measurement perspective this may be treated as another component of the surface current, however. Second, it is known from numerous measurements of the radar modulation transfer function (MTF) [*Keller and Wright*, 1975; *Wright et al.*, 1980; *Plant*, 1989; *Keller et al.*, 1994] that coupling between the amplitude and phase responses of the microwave return due to both geometrical and hydrodynamic sources can lead to a bias in the mean Doppler velocity. This bias is sensitive to the radar orientation to the wind and wave field and can be lessened depending on the processing approach.

To study the azimuthal and resolution dependence of interferometric velocities, a series of short data files with look directions spaced by 15° were collected in the manner illustrated by Figure 7 (top). Obstacles on the pier constrained the range of look directions, so the data collected spanned viewing angles from offshore (70°) to slightly onshore (295°) in a counterclockwise rotation. The total time taken to acquire these files was ~50 min with, on average, 5 min separating successive look directions. During this time, environmental conditions remained fairly stable with winds of 6.8 ± 0.4 m s^{-1} from 352 ± 5°. Dominant waves were from 40° with a period of 5 s.

The data from this sequence are averaged over range and temporally averaged for 80 s to yield mean velocities indepen-

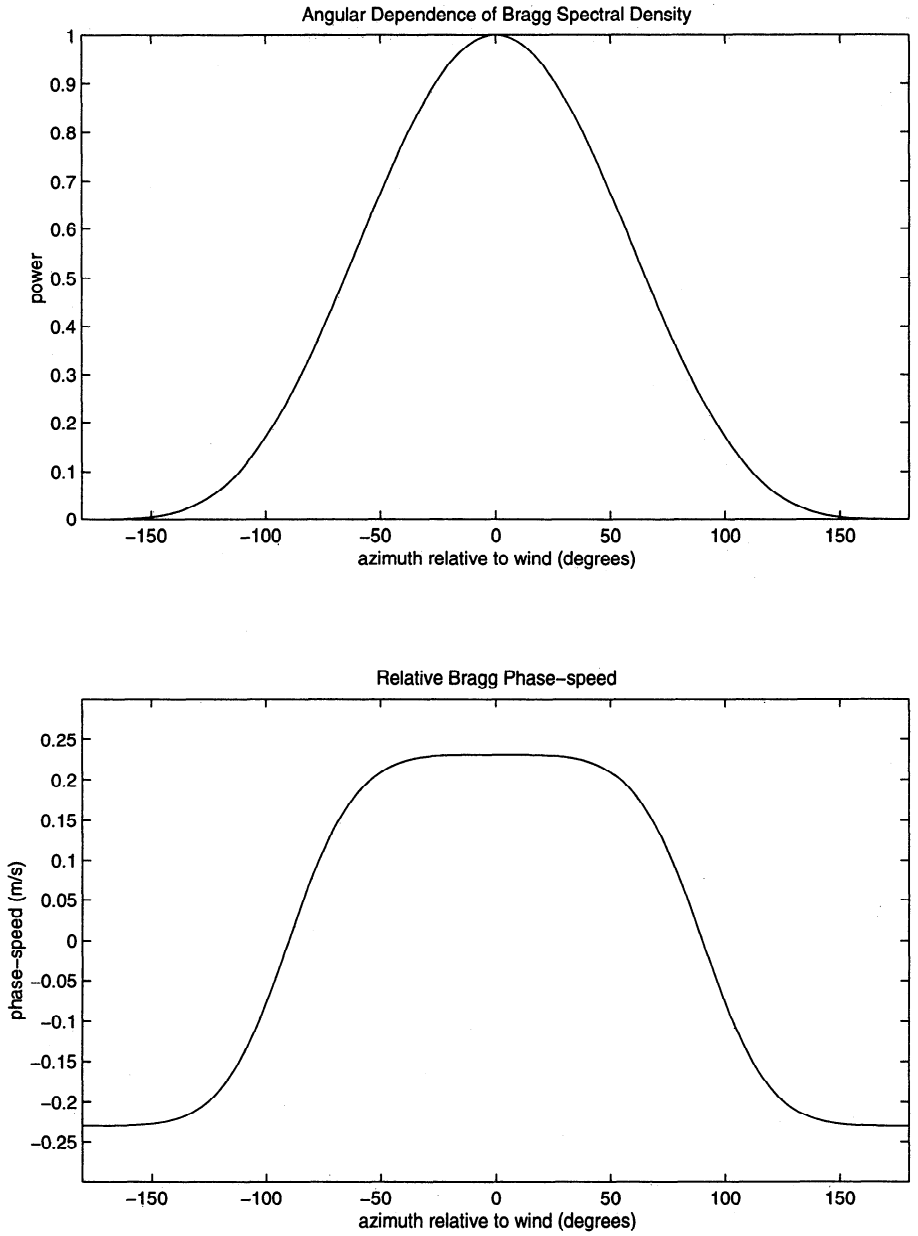

Figure 5. Model for the contribution of Bragg-resonant waves to a surface current measurement. (top) Angular dependence of the short wave power spectral density using (9) with $n = 4$. (bottom) The angular dependence of the measured Bragg velocity as defined in (10).

dent of the wave orbital velocity. In this case, 80 s represents 16 periods of the dominant waves at any given pixel. Assuming that surface wave statistics are ergodic, the combination of spatial and temporal averaging of FOPAIR imagery is roughly equivalent to the larger-scale spatial averaging performed on ATI-SAR data to extract surface currents. It is the averaging method that is evaluated here.

Figure 7 (bottom) shows azimuthal profiles of the mean Doppler velocity for the rotation sequence using three different averaging techniques. In estimating mean Doppler velocities derived from phase measurements, Chapman [*Chapman et al.*, 1994] considered three types of averaging: coherent averaging, coherent averaging over short intervals (with respect to the dominant wave period) followed by incoherent averaging, and incoherent averaging. Mathematically, the first of these can be stated

$$v \propto \arg \langle I(t)I^*(t+\tau)\rangle \tag{12}$$

which is indicated in Figure 7 with solid curves. The dashed curves show the profile of mean velocities estimated from a combination of coherent and incoherent averaging

$$v \propto \langle \arg \langle I(t)I^*(t+\tau)\rangle_{0.25s}\rangle \tag{13}$$

where the coherent integration time is 0.25 s. Dotted curves show the mean velocities which resulted from incoherent averaging only

$$v \propto \langle \arg I(t)I^*(t+\tau)\rangle \tag{14}$$

The mean wind direction is indicated by the vertical dashed line. For each profile the maximum velocity occurs in the upwind direction.

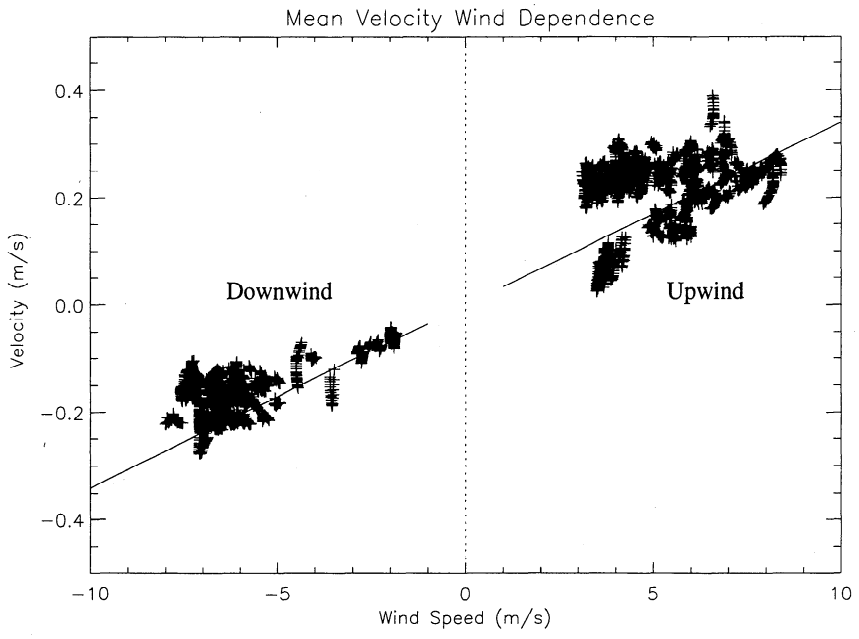

Figure 6. Wind speed dependence of estimated surface wind drag. The solid line shows the assumed characteristic. The dotted line indicates the division between upwind and downwind.

From the upwind region toward offshore directions (70°) the velocity profiles obtained using the processing indicated by (12), (13), and (14) differ with a noticeable trend. At angles $>-30°$, incoherently averaged velocities are up to 0.20 m s^{-1} lower than those derived from a coherent average. These observations can be explained in terms of the MTF, as the portions of the long waves tilted toward the radar contribute more power than other portions biasing the mean velocity toward the higher power regions of the waves. This effect is most pronounced when looking into the wave field, where the approaching regions of the gravity waves will be weighted more heavily than the receding regions, thus incurring a positive velocity bias. This is demonstrated in Figure 7, where the incoherently averaged means are consistently lower than the coherent means, particularly in the upwind/upwave region. Little difference is noticed in the two shoreward looks, which are oblique to the wind and wave field.

Chapman et al. [1994] found that at moderate incidence angles a coherent average over 0.25 s did not incur a significant bias. However, these low grazing angle observations show a further reduction in the mean upwind/upwave velocities when only incoherent averaging is used. As an additional measure of confidence that the incoherent average is the most accurate estimate of the mean velocity, Figure 8 includes a comparison with in situ data. In the rotation sequence, two measurement angles spanned upwind; for these, $v_b = v_p = 0.23$ m s^{-1}. The vertical line shows the upwind direction during each acquisition. The prediction of the surface velocity measurement is generated from

$$v = U_c + U_d + v_p$$

where the ADCP provided in situ measurements of U_c at 2 m depth and the wind drift, U_d, is again approximated by 3.5% of the wind speed. The in situ prediction is an approximate one only, especially given the uncertainty in the wind-drift current that was noted previously; however, we believe that this result helps to give an independent measure of the observed trend in Figure 7. The dotted-dashed line indicates the in situ prediction of v over the field of view. In both cases the mean velocities estimated using only incoherent averaging lie closest to the in situ prediction. These observations suggest that interferometric velocity measurements should be incoherently averaged at the highest possible resolution to obtain the most accurate surface current estimates. Most of the remaining data presented in this paper, however, was processed in real time during data collection with a 0.25-s coherent average for data reduction purposes. For this reason the averaging defined by (13) is applied to the data in the remainder of the paper.

4. Subsurface Radar Current Measurements

In addition to surface radial velocity measurements, FOPAIR has sufficient temporal and spatial resolution to estimate near-surface currents from the dispersion properties of long waves imaged by the radar. When no current is present, linear gravity waves follow the dispersion relation

$$\omega_0 = \sqrt{g|\mathbf{k}| \tanh (|\mathbf{k}|d)}, \tag{15}$$

where $\mathbf{k}$ is the wavenumber of the gravity wave, g is gravitational acceleration, and d is the water depth. This behavior is modified in the presence of a current, $\mathbf{U}$, to become

$$\omega = \omega_0 + \mathbf{U} \cdot \mathbf{k}. \tag{16}$$

Equation 16 states that in the presence of a current $\mathbf{U}$ a gravity wave of wavenumber $\mathbf{k}$ will be advected in the direction of the current, thereby causing a frequency shift in an Eulerian measurement. *Stewart and Joy* [1974] derived a form for the influence of the vertical current structure on wave phase speed

$$U(k) = 2k \int_{-d}^{o} U(z) e^{2kz}\, dz, \tag{17}$$

where $U(k)$ denotes the measured current derived from waves of wavenumber k, and $U(z)$ denotes the true vertical profile of

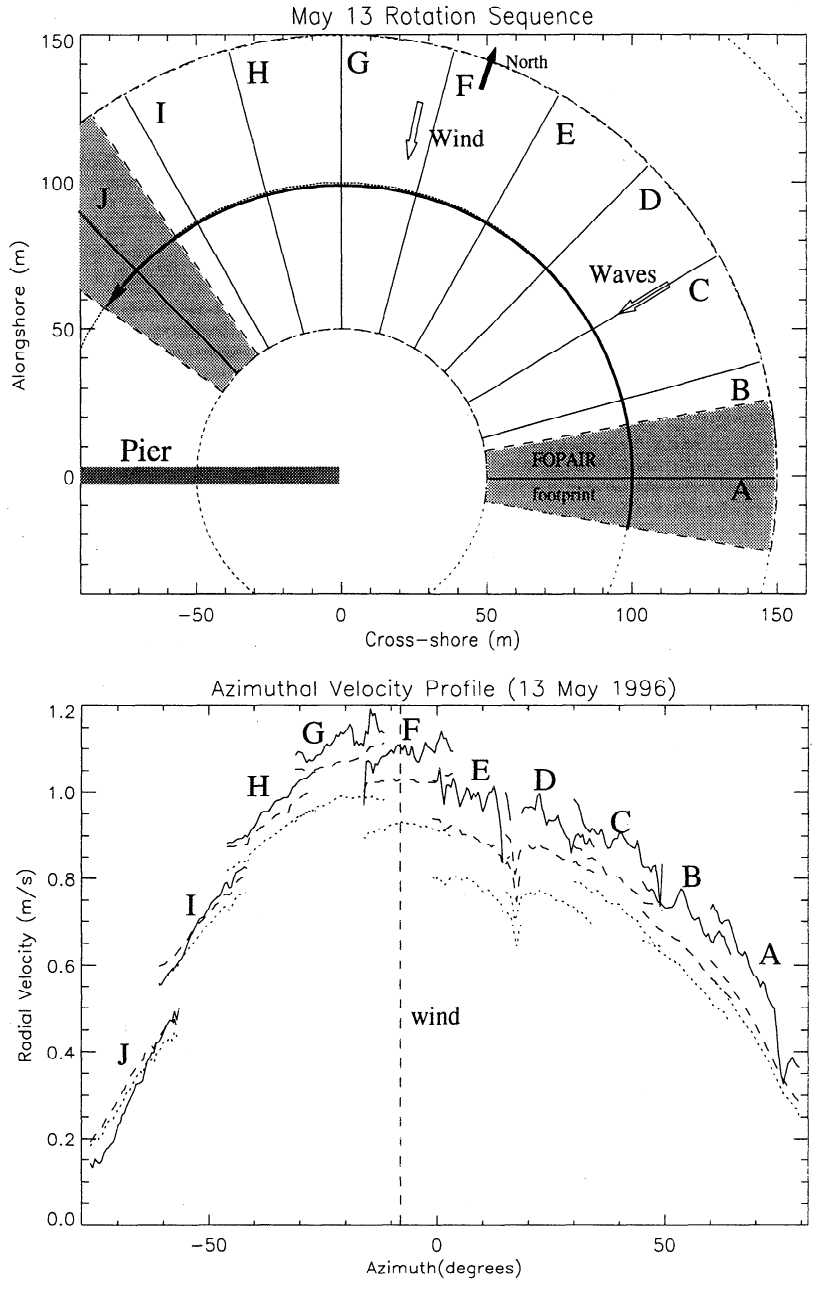

Figure 7. (top) Overview of the experimental site showing sections of ocean surface from which data was obtained. Overlapping image areas were captured in successive collections, rotating counterclockwise from offshore (A–J). The dominant wind and wave directions are shown. (bottom) Velocity profiles as a function of azimuth spanning upwind. Solid curves show coherently averaged velocity. Dashed curves are mean velocity derived from an incoherent average of 0.25-s coherent averages. Dotted curves indicate incoherently averaged velocity. Vertical dashed line is the mean upwind direction during data collection.

current. They showed that under the conditions that U decreases monotonically with depth and is not confined to a layer less than $1/2k$ thick, a measurement $U(k)$ approximately represents the current at a mean depth

$$d_m \simeq \frac{1}{2k} = \frac{\lambda_o}{4\pi}. \tag{18}$$

To extract near-surface current information using (16), FOPAIR imagery is transformed into wavenumber/frequency space as illustrated in Figure 9 [*Frasier and McIntosh*, 1996]. Here the largest circumscribed rectangle about the images is zero padded and Hanning windowed. The power and velocity imagery is then resampled from polar to Cartesian coordinates, and a three-dimensional Fourier transform is applied to 32-s blocks of images. The resulting transform has units of spatial frequency, k_x and k_y, in the x and y directions and temporal frequency, f. Auto- and cross-spectra are accumulated for half-overlapped data segments spanning the total measurement time. A coherence spectrum is then generated from the auto- and cross-spectra according to

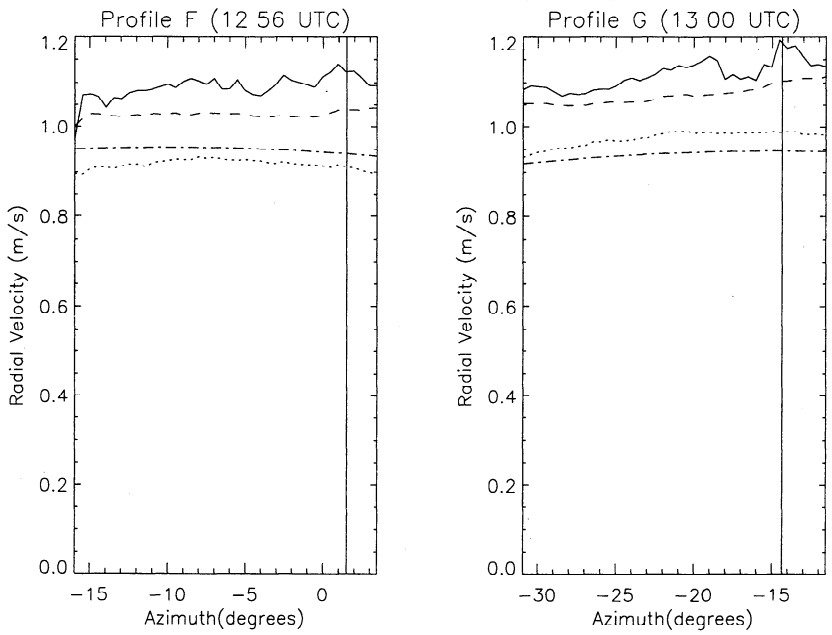

Figure 8. Velocity profiles for two upwind files. Solid curves show coherently averaged mean velocity. Dashed curves are mean velocity from coherent and incoherent averaging. Dotted curves indicate incoherently averaged mean velocity. Dotted-dashed curves show expected velocity estimated from in situ measurements. Vertical solid lines are mean wind direction during data collection.

$$\Gamma^2(k_x, k_y, f) = \frac{|G_{PV}(k_x, k_y, f)|^2}{G_{PP}(k_x, k_y, f) G_{VV}(k_x, k_y, f)} \tag{19}$$

where G_{PP}, G_{VV}, and G_{PV} are the auto- and cross-spectra of power and velocity modulations. This spectrum is particularly useful for observing dispersion relations because it filters out modulations in power and velocity measurements that are not correlated. It is also constrained to lie between values of zero and one.

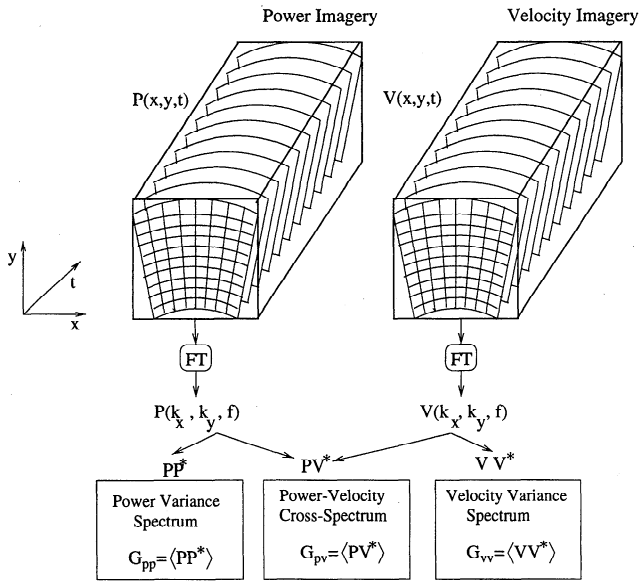

Figure 9. Method by which FOPAIR imagery is transformed into wavenumber/frequency space by applying a three-dimensional Fourier transform applied to a time series of power (P) and velocity (V) imagery. Several spectral products are calculated from the transformed imagery: the power variance spectrum G_{pp}, the power-velocity cross spectrum G_{pv}, and the velocity variance spectrum G_{vv}.

Figure 10 shows constant-frequency slices of the coherence spectrum obtained from a 10-min record when the radar was looking across a strong tidal current. Each panel in this figure is a wavenumber spectrum at a particular frequency. In the absence of a current, modulations due to gravity waves should lie on concentric circles as dictated by the still-water dispersion relation. The distortion of the circles evident in the higher frequency bands is due to the influence of current. The frequency bins $f = 0.469$, 0.531, and 0.594 Hz are overlaid by a solid line, which is the result of a least squares fit of (16) to the wave energy. In the same bins the dotted line shows the still-water dispersion. These frequency bins were selected for current estimation because they show a fairly large degree of directional spreading.

It should be noted that before application of a least squares fit the data is prefiltered for a high coherence and is also prefiltered to exclude the coherent features in the lowest frequency bands likely due to the group behavior of the waves [*Smith et al.*, 1996; *Frasier and McIntosh*, 1996]. The currents derived from the least squares fits are summarized in Table 1, which approximates the mean depths of the currents using (18). Directions given are with respect to the radar orientation.

5. Case Studies of Vertical Current Structure

This section presents several case studies of vertical current structure under differing environmental conditions. For the first profile the radar was oriented upwind and across the current flow. The next profile is generated from imagery acquired when the radar was oriented downwind and viewing a receding tidal current. The final profile presents a case where the radar was oriented downwind with the wind opposing the current.

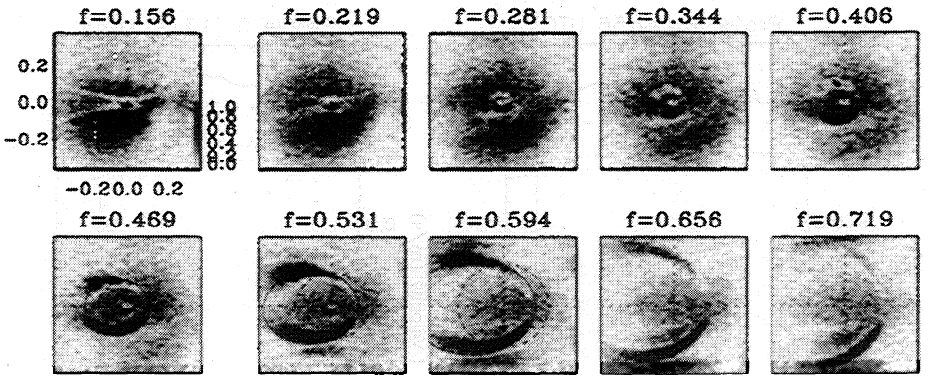

Figure 10. Frequency slices of the coherence spectrum (10-min average) showing the distortion of the dispersion relation due to current. Solid curves show estimated dispersion characteristic in the presence of current. Dashed curves show still-water dispersion.

5.1. Upwind, Cross-Current Profile

The subsurface currents derived from the dispersion characteristics of Figure 10 are combined with ADCP and interferometric measurements to generate the current profiles shown in Figure 11. The radar was looking upwind across a strong tidal current while winds were moderate at 4.3 ± 0.4 m s^{-1}.

To compare radial surface velocity measurements to subsurface current vectors, radial currents, U_r, are plotted as a function of depth in Figure 11 (left). Since the radar is looking across the main tidal flow, subsurface radial velocities are quite low. At the surface, there is a notable positive shift of the current as a direct result of wind drag on the surface. If we assume a 3.5% characteristic for the wind drift and a small radial bulk current contribution, we would expect to measure a surface current of about 16 cm s^{-1}; however, the surface current we observe is 26 cm s^{-1}. We attribute this discrepancy to the inherent variability of surface wind drag as discussed earlier.

A series of vector plots on Figure 11 (right) illustrate the evolution of the current with depth. The surface level shows the radar look direction and the mean wind direction. Radar-derived near-surface current vectors are depicted by the solid arrows while the dashed arrows show the ADCP currents. The overlapping ADCP and radar measurements agree well in both magnitude and direction. The current magnitude steadily increases toward the surface, and a slight rotation in the current direction can be observed. Table 2 summarizes the measurements.

5.2. Downwind, Down-Current Profile

Figure 12 shows a second example where the radar was oriented downwind and down current. The wind was strong at 10.4 ± 0.6 m s^{-1}. Three radar-derived near-surface currents were estimated at mean depths of 0.41, 0.49, and 0.61 m. In the radial velocity profile of Figure 12 (left) the near-surface evolution shows evidence of the wind-induced current penetrating into the water column.

Figure 12 (right) illustrates the vector current evolution. Again, the overlapping radar subsurface and ADCP currents compare well in both magnitude and direction. The vector plot shows the current magnitude increasing toward the surface with a significant clockwise rotation of the current toward the wind direction as the surface is approached. These observations are summarized in Table 3.

5.3. Downwind, Up-Current Profile

The final example shown in Figure 13 was acquired under light winds of 2.4 ± 0.3 m s^{-1} opposing a strong tidal current. Only two radar-derived near-surface currents were extracted from dispersion characteristics corresponding to mean depths of 0.59 and 0.67 m.

This current profile differs significantly from the previous examples. In particular, the current magnitude does not monotonically decrease with depth; instead, several oscillations in the current are noticeable in both the radial velocity and vector plots. The approximation given by (18) for the mean depth of the spectrally derived currents assumes a current whose mag-

Table 1. Currents Estimated From the Dispersion Characteristics of the Cross Spectra for the Upwind, Cross-Current Case

Frequency, Hz	Mean Depth, m	$\|\mathbf{U}\|$, m s^{-1}	$\angle\mathbf{U}$, deg
0.469	0.50	0.51 ± 0.06	5 ± 7
0.531	0.35	0.59 ± 0.04	6 ± 6
0.594	0.29	0.57 ± 0.05	3 ± 6

Table 2. Vertical Profile of Currents for the Upwind, Cross-Current Case Shown in Figure 11

Depth, m	Sensor	$\|\mathbf{U}\|$, m s^{-1}	$\angle\mathbf{U}$, °T	U_r, m s^{-1}
0	FOPAIR	...	...	0.26 ± 0.01
0.29	FOPAIR	0.57 ± 0.05	168 ± 6b	0.03 ± 0.07
0.35	FOPAIR	0.59 ± 0.04	171 ± 6	0.04 ± 0.07
0.50	FOPAIR	0.51 ± 0.06	170 ± 7	0.01 ± 0.07
0.50	ADCP	0.61	168	0.01
1.0	ADCP	0.57	166	−0.01
3.75	ADCP	0.61	167	0.01
4.25	ADCP	0.58	166	−0.01
4.75	ADCP	0.54	164	−0.03
5.25	ADCP	0.51	162	−0.05
5.75	ADCP	0.47	158	−0.07
6.25	ADCP	0.44	155	−0.09
6.75	ADCP	0.40	151	−0.11
7.25	ADCP	0.37	148	−0.12
7.75	ADCP	0.35	144	−0.13

FOPAIR is focused phased array imaging radar, and ADCP is acoustic Doppler current profiler.

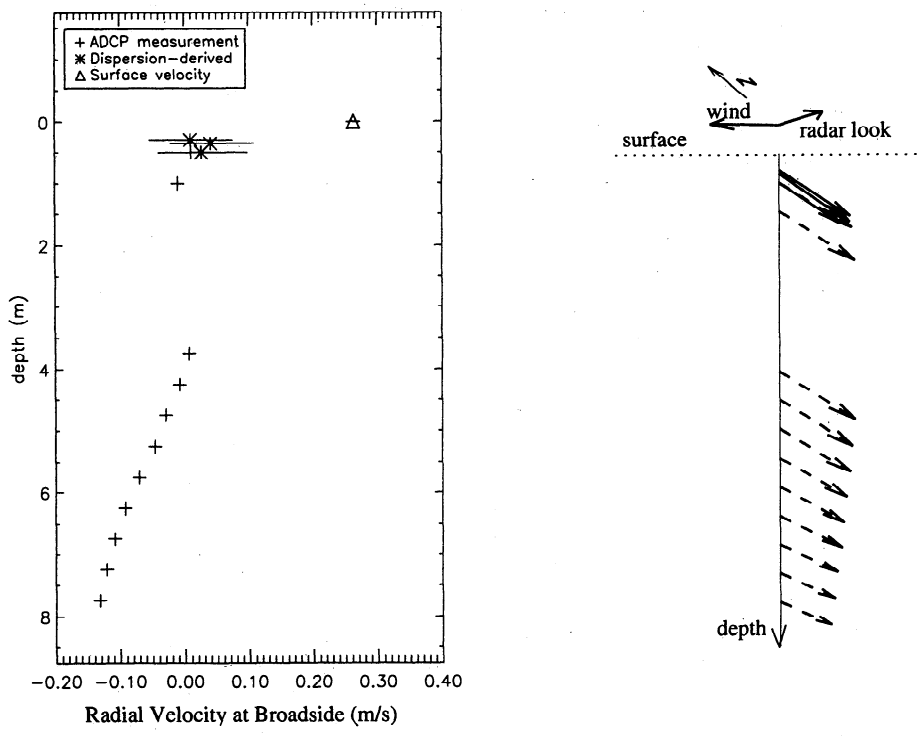

Figure 11. Vertical profile of current structure when the radar is oriented upwind and cross current. (left) Current evolution in the radar line-of-sight direction. (right) The series of vectors show the evolution of the current with depth.

nitude monotonically decreases with depth. That condition does not pertain in this case, so the mean depths were estimated directly from (17) using the ADCP measurements as samples of $U(z)$.

In the radial velocity profile, there is little difference between the surface current and the near-surface currents. Since the wind conditions are light, the wind-drift component of the surface current is small. The interferometric surface current lies close to the ground truth estimate. Table 4 tabulates the current profile for this case.

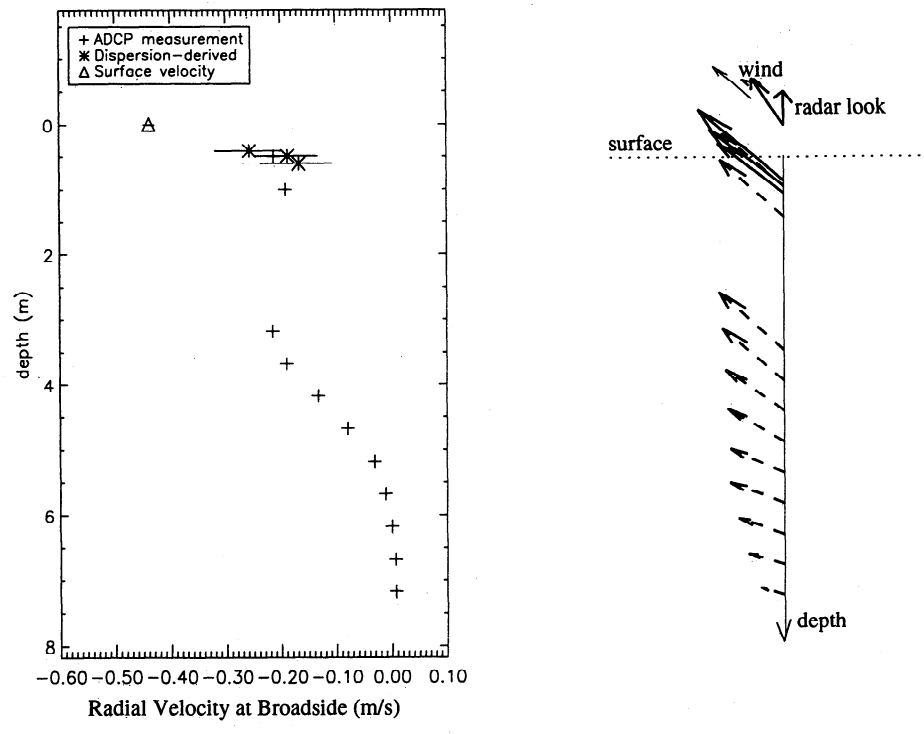

Figure 12. Same as Figure 11, but when the radar is oriented downwind and down current.

Table 3. Vertical Profile of Currents for the Downwind, Down-Current Case Shown in Figure 12

Depth, m	Sensor	|U|, m s^{-1}	∠U, °T	U_r, m s^{-1}
0	FOPAIR	...	...	−0.44 ± 0.01
0.41	FOPAIR	0.34 ± 0.05	001 ± 6	−0.26 ± 0.06
0.49	FOPAIR	0.27 ± 0.05	356 ± 7	−0.19 ± 0.06
0.50	ADCP	0.27	004	−0.21
0.61	FOPAIR	0.24 ± 0.06	356 ± 8	−0.17 ± 0.07
1.0	ADCP	0.25	002	−0.19
3.18	ADCP	0.27	004	−0.21
3.68	ADCP	0.25	002	−0.19
4.18	ADCP	0.20	353	−0.13
4.68	ADCP	0.17	340	−0.08
5.18	ADCP	0.14	324	−0.03
5.68	ADCP	0.14	317	−0.01
6.18	ADCP	0.12	312	0.00
6.68	ADCP	0.10	308	0.01
7.18	ADCP	0.06	305	0.01

Table 4. Vertical Profile of Currents for the Downwind, Up-Current Case Shown in Figure 13

Depth, m	Sensor	|U|, m s^{-1}	∠U, °T	U_r, m s^{-1}
0	FOPAIR	...	...	0.40 ± 0.01
0.50	ADCP	0.45	157	0.45
0.59	FOPAIR	0.40 ± 0.05	164 ± 10	0.39 ± 0.06
0.67	FOPAIR	0.36 ± 0.04	166 ± 12	0.35 ± 0.07
1.0	ADCP	0.36	154	0.36
2.20	ADCP	0.46	157	0.46
2.70	ADCP	0.38	154	0.38
3.20	ADCP	0.35	159	0.35
3.70	ADCP	0.41	165	0.41
4.20	ADCP	0.46	168	0.45
4.70	ADCP	0.44	167	0.43
5.20	ADCP	0.38	168	0.37
5.70	ADCP	0.31	168	0.30
6.20	ADCP	0.21	167	0.21

5.4. FOPAIR and ATI-SAR Comparison

ERIM overflew the FRF site during the May experiment with an X-band (9.66 GHz) ATI-SAR. During these overflights the ATI-SAR operated in spotlight mode from an altitude of ~4 km at an incidence angle of 45°. For these collections the ATI-SAR was directed along the pier axis looking seaward (70°T). At a nominal aircraft speed the effective pulse-pair interval was 4.7 ms.

At the same time, FOPAIR acquired data with the same viewing orientation and with a pulse-pair interval of 5.5 ms, comparable to the equivalent delay of the ATI-SAR. Coincident surface current estimates derived from FOPAIR and the ATI-SAR were collected on two separate occasions. In each case the radars were looking obliquely upwind; therefore we assumed that the Bragg-resonant waves were approaching the radars.

ATI-SAR radial surface currents were derived from the mean phase of a region approximately 300 × 400 m^2. The averaged region extends beyond the end of the pier and encompasses the FOPAIR footprint. The nominal spatial resolution of the SAR was set at 30 cm in range and 23 cm in azimuth (These are the resolutions dictated by the signal processing; the true azimuthal resolution is much coarser and is determined primarily by the coherence time of the ocean surface scattering. We estimate that true azimuthal resolution is ~50 m). Interferometric phases in the SAR imagery were coherently averaged over 6 × 6 pixel neighborhoods, yielding effective pixel sizes of 1.77 m in range and 1.35 m in azimuth. Phases were then converted to horizontal velocities and compensated for the Bragg phase speed.

The FOPAIR surface current measurements resulted from a combination of incoherent and coherent averaging also. Velocities were derived from the phases of 0.25-s coherent averages and then further averaged over range and temporally for

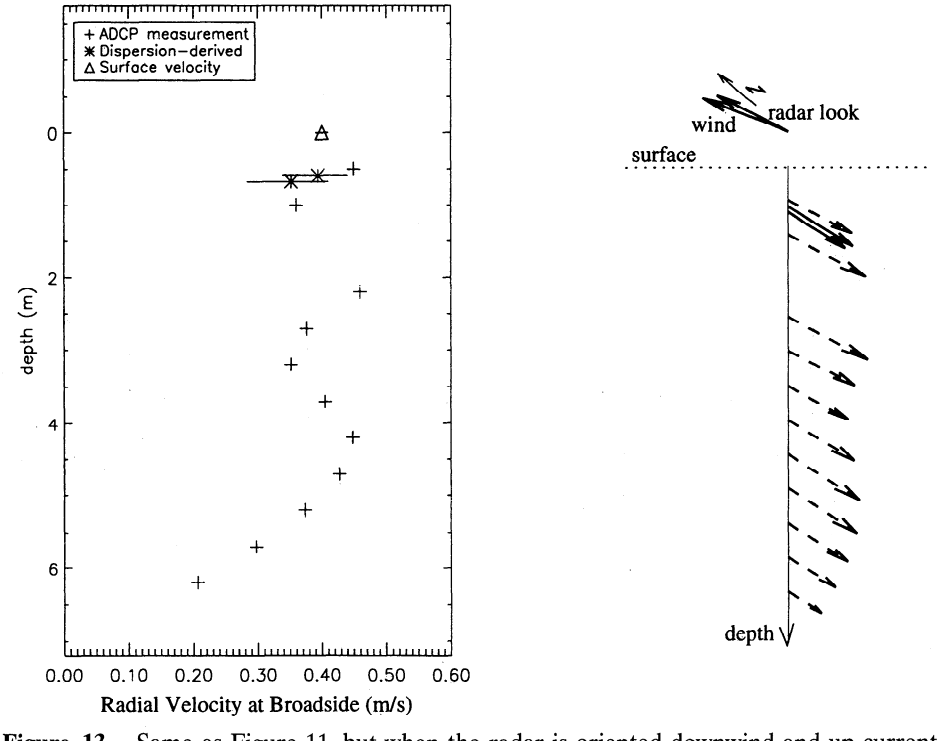

Figure 13. Same as Figure 11, but when the radar is oriented downwind and up current.

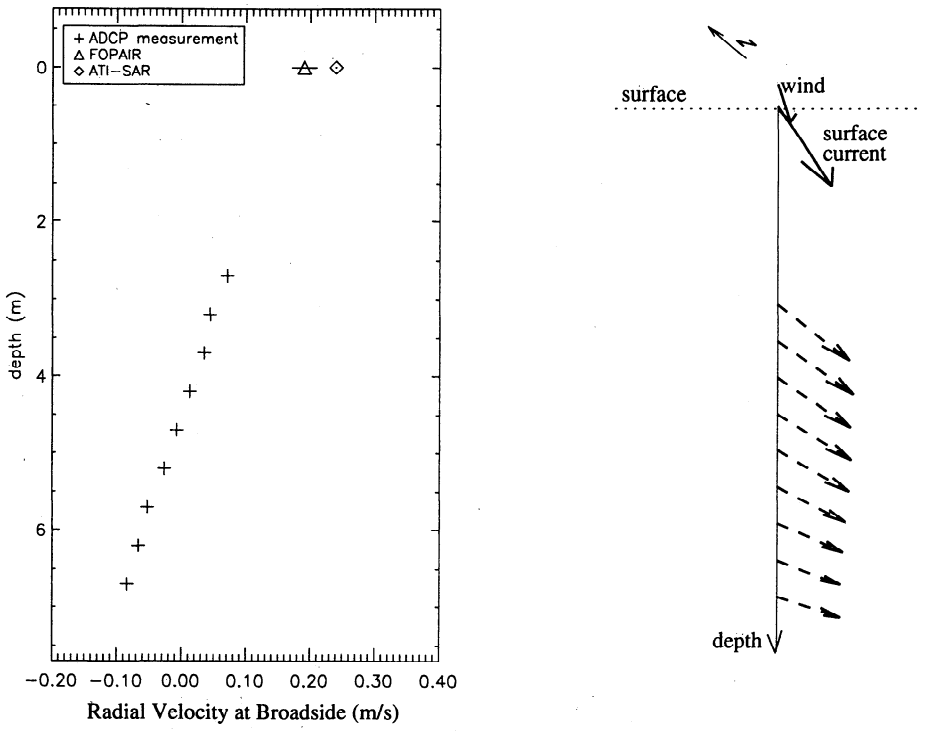

Figure 14. Same as Figure 11, but during along-track interferometric synthetic aperture radar overflight.

20 s, after which the phase speed of the Bragg-resonant waves was subtracted from the mean velocity.

In the first case, FOPAIR measured a surface current of 0.21 ± 0.53 m s^{-1}, and the ATI-SAR measured 0.15 ± 0.50 m s^{-1}. In this case the variance measure quoted is the variance due to the wave orbital velocities observed within the imagery, not a variance of the mean which was quoted for the previous surface measurements. While the mean currents are close, it is also significant that the variances are similar, showing that the two systems incur the same degree of frequency modulation from the wave orbital velocities. This is also true for the second comparison where FOPAIR measured 0.19 ± 0.33 m s^{-1} and the ATI-SAR measured 0.24 ± 0.29 m s^{-1}.

On May 14, directly following the overflight of the ATI-SAR, FOPAIR was rotated 90° counterclockwise to look alongshore (340°T). Surface currents generated from consecutive orthogonal acquisitions were combined to yield a vector surface current measurement. The composite of this surface vector, the ATI-SAR radial current, and ADCP subsurface current measurements is illustrated in the plots of Figure 14. Figure 14 (left) shows the evolution of the current along the ATI-SAR viewing direction (70°T). A clear increase occurs in the ADCP currents toward the surface. The FOPAIR and ATI-SAR surface currents are very close. Because of surface wind drag the interferometric measurements are greater than the subsurface currents. No radar-derived near-surface currents were possible in this case as the FOPAIR records obtained during the overflights were short, and the available averaging time was insufficient to extract a good estimate using this technique.

Figure 14 (right) compares the interferometric surface current vector to the subsurface measurements. The surface vector is nearly aligned with the wind direction. As the currents approach the surface, they increase in magnitude and rotate clockwise toward the wind direction. These observations are summarized in Table 5.

Table 5. Vertical Profile of Currents During the May 14 ATI-SAR Overflight Shown in Figure 14

Depth, m	Sensor	$\|\mathbf{U}\|$, m s^{-1}	$\angle\mathbf{U}$, °T	U_r, m s^{-1}
0	ATI-SAR	...	...	0.24
0	FOPAIR	0.39	201	0.19
2.70	ADCP	0.27	177	0.07
3.20	ADCP	0.26	171	0.04
3.70	ADCP	0.24	170	0.03
4.20	ADCP	0.23	165	0.01
4.70	ADCP	0.21	159	−0.01
5.20	ADCP	0.19	154	−0.03
5.70	ADCP	0.18	144	−0.05
6.20	ADCP	0.17	138	−0.07
6.70	ADCP	0.17	131	−0.08

ATI-SAR is along-track interferometric synthetic aperture radar.

6. Summary and Discussion

In this paper we explored the relationship between interferometric velocity measurements and current flow in the water column. First, the components of an interferometric velocity were detailed showing how to extract the surface current from these measurements. Most significantly, a model for the angular dependence of the Bragg velocity was closely approximated by data estimates of the same quantity. This is significant because uncertainty in the Bragg velocity can be a substantial source of error for measurements off the wind axis. Establishing a functional form for the Bragg contribution to interferometric velocities is important for surface current measurements.

Second, azimuthal profiles of the mean velocity through the wind and wave field showed that a mean velocity computed by a coherent integration over the entire data set can be biased toward the velocity of the high-return region of the modulating waves. This effect is due to coupling between the amplitude and frequency modulations of the backscattered field and is

particularly evident in the upwind/up-wave directions. It is therefore recommended that the mean velocity be generated by averaging velocities obtained on the finest timescale possible, effectively decoupling the amplitude and frequency modulations of the backscatter.

Three examples of vertical current profiles were presented for different environmental conditions and radar orientations. In these case studies several near-surface currents were estimated from the dispersion characteristics of FOPAIR imagery. These subsurface currents compared well with ADCP measurements, and the combination of the two created a uniquely detailed view of the current in the upper meter of the ocean.

These case studies clearly demonstrate the potent effect of the wind on surface velocity measurements at X-band radar frequencies. When a consistently strong wind was present, the wind-driven current penetrated significantly into the water column. In this situation an interferometric surface current is not merely a wind-drift measurement but is an indication of water movement beyond the surface layer. When winds were low to moderate, however, there was no noticeable subsurface penetration of the surface wind-drift current.

The similarity of interferometric measurements made by FOPAIR and ATI-SAR confirms that this analysis of FOPAIR current measurements is relevant to ATI-SAR interpretation. During an ATI-SAR overflight an interferometric surface current vector was derived from FOPAIR data using consecutive orthogonal acquisitions. This vector was closely aligned with the wind direction as expected. When compared with subsurface ADCP currents, we observed that approaching the surface, the current increased in magnitude and rotated toward the wind direction.

In summation, these results utilized FOPAIR's temporal and spatial resolution capabilities, presenting uniquely detailed observations of radar current measurements in relationship to the physical environment. The study of the Bragg phase speed and wave orbital velocity provides valuable information for ATI-SAR processing of surface velocities. Furthermore, the vertical current profiles demonstrate how representative surface currents are of bulk water movement in the coastal regime.

Acknowledgments. The authors gratefully acknowledge R. Chapman, D. Thompson, B. Gotwols, M. Jose, and R. Sterner of JHU/APL; M. Sletten of NRL; and J. Eshbaugh and J. Li of UMass for their support in the field and in the laboratory. We acknowledge the Environmental Research Institute of Michigan and thank Chris Wackerman for providing comparative measurements from their interferometric SAR system. The staff at the Army Corps of Engineers Field Research Facility, whose facilities we utilized, deserve special mention for their logistical support and accommodation. This work was supported by the Office of Naval Research (Remote Sensing) under grant N00014-95-1-0832.

References

Ainsworth, T. L., S. R. Chubb, R. Fusina, R. Goldstein, R. Jansen, J. Lee, and G. Valenzuela, INSAR imagery of surface currents, wave fields, and fronts, *IEEE Trans. Geosci. Remote Sens.*, *33*(5), 1117–1122, 1995.

Alpers, W., and K. Hasselmann, The two-frequency microwave technique for measuring ocean-wave spectra from airplane and satellite, *Boundary Layer Meteorol.*, *13*, 215–230, 1978.

Barrick, D. E., First order theory and analysis of mf/hf/vhf scatter from the sea, *IEEE Trans. Antennas Propag.*, *20*(1), 2–10, 1972.

Chapman, R. D., B. L. Gotwols, and R. E. Sterner II, On the statistics of the phase of microwave backscatter from the ocean surface, *J. Geophys. Res.*, *99*(C8), 16,293–16,301, 1994.

Fernandez, D. M., J. F. Vesecky, and C. C. Teague, Measurements of upper ocean surface current shear with high-frequency radar, *J. Geophys. Res.*, *101*(C12), 28,615–28,625, 1996.

Frasier, S. J., and R. E. McIntosh, Observed wavenumber-frequency properties of microwave backscatter from the ocean surface at near-grazing angles, *J. Geophys. Res.*, *101*(C8), 18,391–18,407, 1996.

Goldstein, R. M., T. P. Barnett, and H. A. Zebker, Remote sensing of ocean currents, *Science*, *246*, 1282–1285, 1989.

Graber, H. C., D. R. Thompson, and R. E. Carande, Ocean surface features and currents measured with synthetic aperture radar interferometry and HF radar, *J. Geophys. Res.*, *101*(C11), 25,813–25,832, 1996.

Heron, M. L., Directional spreading of short wavelength fetch-limited wind waves, *J. Phys. Oceanogr.*, *17*, 281–285, 1987.

Keller, W. C., and J. W. Wright, Microwave scattering and the straining of wind-generated waves, *Radio Sci.*, *10*, 139–147, 1975.

Keller, W. C., W. J. Plant, R. A. Petitt Jr., and E. A. Terray, Microwave backscatter from the sea: Modulation of received power and Doppler bandwidth by long waves, *J. Geophys. Res.*, *99*(C5), 9751–9766, 1994.

Kinsman, B., *Wind Waves*, Prentice-Hall, Englewood Cliffs, N. J., 1965.

Lange, P., and H. Huhnerfuss, Drift response of monolayer slicks to wave and wind action, *J. Phys. Oceanogr.*, *8*, 142–150, 1978.

Lyzenga, D. R., Interaction of short surface and electromagnetic waves with ocean fronts, *J. Geophys. Res.*, *96*(C6), 10,765–10,772, 1991.

Marmorino, G. O., D. R. Thompson, H. C. Graber, and C. L. Trump, Correlation of oceanographic signatures appearing in synthetic aperture radar and interferometric synthetic aperture radar imagery with in situ measurements, *J. Geophys. Res.*, *102*(C8), 18,723–18,736, 1997.

McIntosh, R., S. Frasier, and J. Mead, FOPAIR: A focused phased array imaging radar for ocean remote sensing, *IEEE Trans. Geosci. Remote Sens.*, *33*(1), 115–124, 1995.

Miller, K., and M. Rochwarger, A covariance approach to spectral moment estimation, *IEEE Trans. Inf. Theory*, *18*(5), 588–596, 1972.

Plant, W., Studies of backscattered sea return with a CW, dual-frequency, X-band radar, *IEEE Trans. Antennas Propag.*, *25*(1), 28–36, 1977.

Plant, W., The modulation transfer function: Concept and applications, in *Radar Scattering From Modulated Wind Waves*, edited by J. Komen, W. Oost, pp. 155–172, Kluwer Acad., Norwell, Mass., 1989.

Plant, W., Bragg scattering of electromagnetic waves from the air/sea interface, in *Surface Waves and Fluxes*, vol. 2, *Remote Sensing*, edited by G. L. Geernaert and W. J. Plant, chap. 11, pp. 41–108, Kluwer Acad., Norwell, Mass., 1990.

Popstefanija, I., and R. E. McIntosh, Measurements of the effects of surface winds on ocean currents with a stepped-frequency ΔK radar system, *J. Geophys. Res.*, *97*(C4), 5597–5605, 1992.

Schuler, D. L., Remote sensing of directional gravity wave spectra and surface currents using a microwave dual-frequency radar, *Radio Sci.*, *13*, 321–331, 1978.

Shemer, L., M. Marom, and D. Markman, Estimates of currents in the nearshore ocean region using interferometric synthetic aperture radar, *J. Geophys. Res.*, *98*(C4), 7001–7010, 1993.

Smith, M. J., E. M. Poulter, and J. A. McGregor, Doppler radar measurements of wave groups and breaking waves, *J. Geophys. Res.*, *101*(C6), 14,269–14,282, 1996.

Stewart, R. H., and J. W. Joy, HF radio measurements of surface currents, *Deep Sea Res. Oceanogr. Abstr.*, *21*, 1039–1049, 1974.

Thompson, D., Calculation of microwave Doppler spectra from the ocean surface with a time-dependent composite model, in *Radar Scattering From Modulated Wind Waves*, edited by G. Komen and W. Oost, pp. 27–40, Kluwer Acad., Norwell, Mass., 1989.

Thompson, D. R., and J. R. Jensen, Synthetic aperture radar interferometry applied to ship-generated internal waves in the 1989 Loch Linnhe experiment, *J. Geophys. Res.*, *98*(C6), 10,259–10,269, 1993.

Wright, J. W., W. J. Plant, W. C. Keller, and W. L. Jones, Ocean wave-radar modulation transfer functions from the West Coast Experiment, *J. Geophys. Res.*, *85*(C9), 4957–4966, 1980.

S. J. Frasier and R. E. McIntosh, Microwave Remote Sensing Laboratory, University of Massachusetts, Amherst, MA 01003. (e-mail: frasier@alex.ecs.umass.edu)

D. Moller, Jet Propulsion Laboratory, 4800 Oak Grove Drive, Pasadena, CA 91109. (e-mail: moller@muscovy.jpl.nasa.gov)

D. L. Porter, Applied Physics Laboratory, Johns Hopkins University, Laurel, MD 20723-6099.

(Received August 4, 1997; revised February 12, 1998; accepted March 9, 1998.)